CSIRO PUBLISHING

Exploration Geophysics
http://dx.doi.org/10.1071/EG15070

3D inversion of total magnetic intensity data for time-domain EM at the Lalor massive sulphide deposit

Dikun Yang[1,2] Douglas W. Oldenburg[1]

[1]Geophysical Inversion Facility, Department of Earth, Ocean and Atmospheric Sciences, University of British Columbia, 2020-2207 Main Mall, Vancouver, British Columbia, Canada V6T 1Z4.
[2]Corresponding author. Email: yangdikun@gmail.com

Abstract. The Lalor deposit is a massive sulphide that is characterised as a stack of conductive ore lenses buried more than 600 m deep. We invert helicopter sub-audio magnetics (HeliSAM) data from Lalor collected using a ground large transmitter loop and an airborne total magnetic intensity (TMI) magnetometer measuring the time-domain electromagnetic (EM) responses. The TMI data are modelled as a projection of the anomalous field onto the earth's magnetic field. Inversion of these data is considered a significant case study because of two challenges. First, the early-time data are contaminated by the infrastructure on the surface. Second, inverting the data with a uniform half-space as the initial model results in a mathematically acceptable, but non-geologic, model. We create workflows to overcome these difficulties. For the contaminated data, we use a locally refined mesh and a constrained inversion to recover highly conductive cells near the surface that effectively represent the infrastructure. This allows us to safely extract geologic information from the early time data. The non-uniqueness in the inversion is reduced by warm-starting the voxel 3D inversion with a more reasonable initial guess, for example, a block model from geometric inversions. Those procedures greatly improve the inversion image from the surface to the bottom of the target at Lalor, and they can easily be incorporated into the industrial production workflows.

Key words: 3D inversion, Lalor, mineral exploration, time-domain electromagnetic, total magnetic intensity, volcanogenic massive sulphide.

Received 24 July 2015, accepted 5 December 2015, published online 13 January 2016

Introduction

The Lalor deposit is located within the meta-volcanics, meta-sediments and granitoids of the Churchill province in the Flin Flon Greenstone Belt, and is ~8 km west of Snow Lake in central Manitoba, Canada (Figure 1). The deposit, discovered in 2007 in the Chisel Basin that hosts another five mines, is believed to be the largest volcanogenic massive sulphide (VMS) ever found in this area. Following the initial discovery made by geophysics, an extensive drilling program has revealed that the deposit comprises many discrete ore lenses stacked together. The upper lenses, from 600 to 1000 m deep, are zinc-rich, and have high concentrations of pyrite in the form of near-solid sulphide. The lower lenses, below 1000 m deep, are mostly stringer sulphides with a high grade of gold and gold-copper concentration. After the mineralisation, the Chisel Basin was also subject to the deformation that has made all the ore lenses dip ~30° to north (Figure 2). Disseminated sulphides are also found around the ore lenses as a result of alteration in the host rock (Taylor, 2014).

Given its world-class reserves, the development of the Lalor Mine was fast-tracked. The construction of infrastructure at Lalor started in 2009, and full-scale development was committed in 2010. In 2012, the ventilation shaft was finished to enable the initial ore production. Production from the main shaft began in the second half of 2014, marking the complete finish of mine construction. Although the fast development was responsible for many drill holes that have delineated the main target in great detail, prospectors still have questions regarding the extension of the mineralised zone and whether there are other economically interesting targets nearby. The geologic and geophysical surveys carried out for the continued discovery of new mineralisation during the mine construction also serve as a good example of brown-field exploration.

Because of the abundance of sulphide in the ore body the Lalor deposit is geophysically characterised as a deeply buried good conductor that exhibits electrical responses that are distinct from the relatively resistive background. Since the initial discovery by deeply penetrating electromagnetic (EM) surveys, the Lalor deposit has been a test bed for a variety of EM systems that represent the state-of-the-art techniques in mineral exploration. To our best knowledge, there are at least 15 different EM datasets at Lalor collected from the air, on the surface and in boreholes. The large amount of EM data at Lalor has recently drawn particular attention in the mining geophysics community. Three symposia on Lalor have been held by the British Columbia Geophysical Society (Vancouver), the Manitoba Mining and Minerals Convention (Winnipeg), and the Canadian Exploration Geophysical Society (Toronto) in 2014. The South African Geophysical Association also hosted a special session on Lalor in 2015. We at the University of British Columbia have been actively working on the interpretation of some of the datasets using our 3D inversion algorithms (Yang and Oldenburg, 2012*b*, 2013).

The controlled source EM surveys at Lalor fall into two streams: (1) the airborne coincident loop EM provides great regional coverage but the data may suffer from low signal-to-noise ratio (SNR), especially for the late-time channels, because

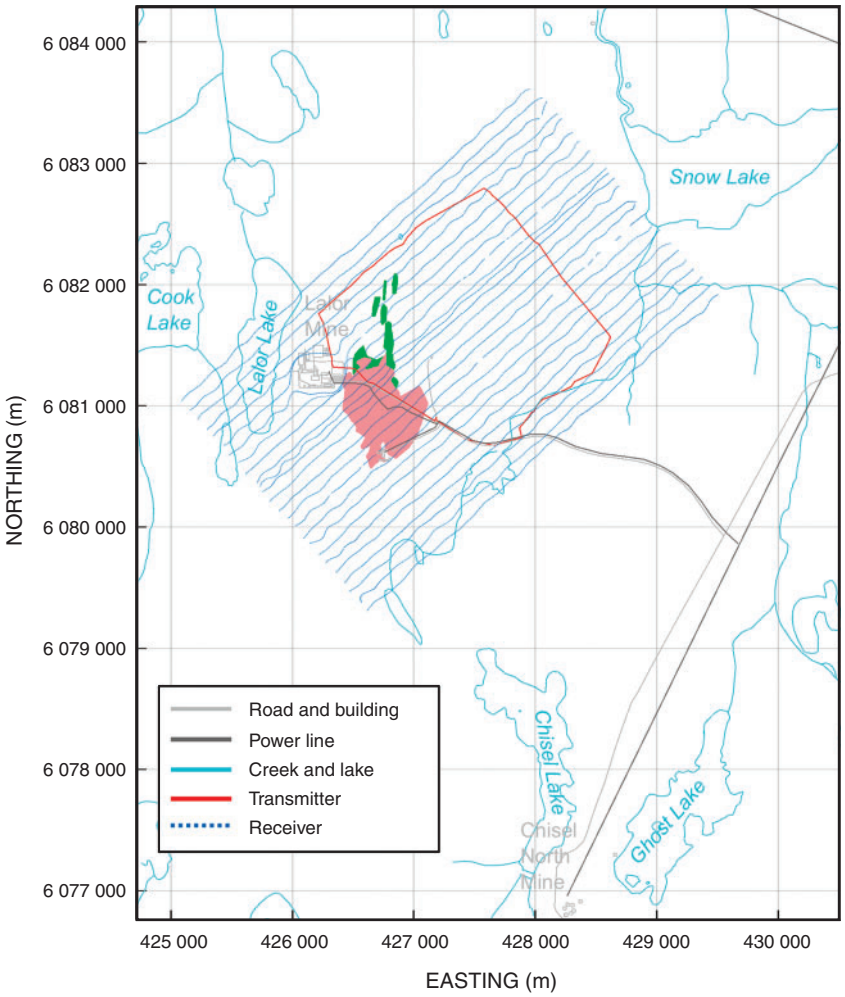

Fig. 1. Geographic map of the Lalor deposit and the HeliSAM survey layout. The drilled ore lenses are projected onto the surface shown as pink and green polygons.

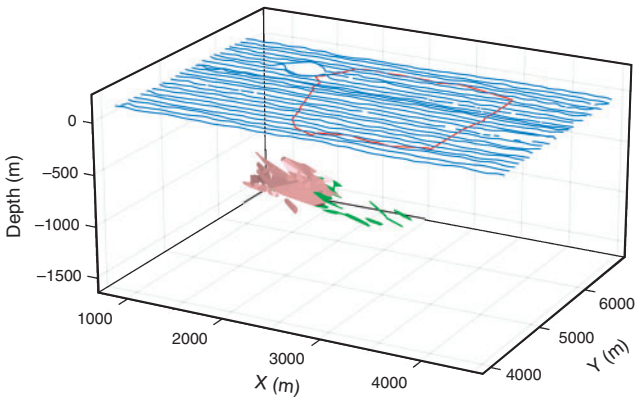

Fig. 2. The 3D ore lenses model at Lalor and the HeliSAM survey layout in local coordinate system. Two types of sulphide at Lalor, near-solid and stringer, are coloured in pink and green respectively.

of relatively small transmitter moment and the movement of the platform; (2) the ground large-loop surveys can generate a much greater primary field, yielding signals of good quality, but the receiver locations are usually confined to a few lines on the surface or down the boreholes. The helicopter sub-audio magnetics (HeliSAM) system (a product of Gap Geophysics Australia) is configured to address these issues. It employs a large ground loop fixed on the surface as the transmitter to enhance the strength of signals, and flies a caesium vapour magnetometer (B-field SAM sensor) over the area to collect the transient magnetic field data. Because the magnetometer measures the scalar total magnetic intensity (TMI) like in the magnetic survey, the data are insensitive to the orientation of the towed bird, so the quality of data is higher than in the conventional airborne EM. In addition, when mapping good conductors, the B-field data have advantages over the dB/dt data acquired by most airborne time-domain EM (TEM) systems (Smith and Annan, 1998).

In this paper, we present some background about HeliSAM data and a methodology for inverting them. Because the early times are contaminated with EM noise from near-surface infrastructure, it is usual to discard those data and invert the late-time data only. For Lalor this seems reasonable because the sought bodies are deeply buried. However, that approach discards conductivity information about the near surface and this has implications for non-uniqueness when inverting late-time data only. We tackle this problem by working with a fine-scale mesh and inverting only early times to obtain the near-surface structure and then incorporate that information into a larger problem where all time channels are inverted. An additional challenge is that, for highly conductive objects buried in a resistive host, voxel inversions can fit the data with a complicated, non-geologic structure. A remedy is to carry out the inversion in two stages. The first is to find an approximate location for a highly conductive target, and then to use that for a warm-start for a traditional voxel inversion. We show the practicality of this for the Lalor Deposit. The paper finishes with comments and discussion.

HeliSAM survey at Lalor

HeliSAM system

The SAM sensor is a caesium vapour magnetometer that measures the total magnetic field, which is the magnitude of the combination of three vector fields: the earth's regional magnetic field ($\mathbf{B}_0$), the local magnetic anomaly due to the magnetic susceptibility ($\mathbf{B}_a$), and the magnetic field from the EM induction ($\mathbf{B}_{em}$). Since the earth's magnetic field is much stronger than any other component, the difference between the raw data and the known $\mathbf{B}_0$ can be approximated by the projection of $\mathbf{B}_a + \mathbf{B}_{em}$ onto $\mathbf{B}_0$, so we have

$$\begin{aligned} |\mathbf{B}_0 + \mathbf{B}_a + \mathbf{B}_{em}| - |\mathbf{B}_0| &\approx (\mathbf{B}_a + \mathbf{B}_{em}) \cdot \hat{\mathbf{B}}_0 \\ &= \mathbf{B}_a \cdot \hat{\mathbf{B}}_0 + \mathbf{B}_{em} \cdot \hat{\mathbf{B}}_0. \end{aligned} \quad (1)$$

If the transmitter waveform flips the polarity, the EM fields change the sign but $\mathbf{B}_0$ and $\mathbf{B}_a$ remain the same

$$\begin{aligned} |\mathbf{B}_0 + \mathbf{B}_a - \mathbf{B}_{em}| - |\mathbf{B}_0| &\approx (\mathbf{B}_a - \mathbf{B}_{em}) \cdot \hat{\mathbf{B}}_0 \\ &= \mathbf{B}_a \cdot \hat{\mathbf{B}}_0 - \mathbf{B}_{em} \cdot \hat{\mathbf{B}}_0. \end{aligned} \quad (2)$$

Then the processed data for EM interpretation can be obtained by stacking the measured raw data from opposite polarities

$$\mathbf{B}_{em} \cdot \hat{\mathbf{B}}_0 = \frac{1}{2}(|\mathbf{B}_0 + \mathbf{B}_a + \mathbf{B}_{em}| - |\mathbf{B}_0 + \mathbf{B}_a - \mathbf{B}_{em}|). \quad (3)$$

The final HeliSAM data only contain the EM induced magnetic field projected onto $\hat{\mathbf{B}}_0$, and do not suffer influences from the regional magnetic field and the local susceptibility.

Survey configuration

The layout of the HeliSAM survey is illustrated in Figure 1. It is underlain by the geographic map and the locations of the infrastructure on the site when the survey was taking place in September 2014. The large single-turn transmitter loop, measuring ~1.7 km on the side, is fixed on the flat surface and transmits bipolar square wave of 50% duty cycle at a base frequency of 7.5 Hz using a Phoenix TXU30 transmitter. The 20-A waveform has a turn-off ramp of 0.4 ms, and 16 time channels of TMI data are sampled from 0.42 to 27 ms after the end of the ramp-off. An R44 helicopter tows a TM-7 SAM receiver and flies along 25 profile lines that are spaced 100 m apart. The receiver has a nominal height ~40 m above the ground level. The processed dataset after stacking contains 18 150 receiver locations with station spacing of ~5 m.

The HeliSAM receivers are positioned using GPS within a Universal Transverse Mercator (UTM) coordinate system (easting-northing-elevation), but the flight lines are aligned with a local grid (x–y–z) used by other surface surveys and mining activities. We therefore re-position the HeliSAM survey using the local coordinate system as shown in Figure 2. The coordinate transformation involves a rotation of 42° clockwise, followed by a translation shift in both x and y directions. The vertical positioning of the survey and model are also adjusted from elevation above sea level (ASL) to depth (z) by referencing $z = 0$ to 305 m ASL, an estimated mean value of surface elevation at Lalor.

Field data

The data maps of four time channels (TC), 1, 7, 8, and 16, are presented in Figure 3. The dominant feature on TC 1 is a linear trace of negative–positive with extremely high magnitude that correlates well with the road and power line. This linear feature decays rapidly in time and vanishes before TC 8. These observations imply that those signals are likely caused by the near-surface infrastructure, particularly the power line. The late times from TC 8 to 16 have consistent long-lasting anomalous signals in a compact shape that indicates the main deposit of interest. This field dataset has been preliminarily interpreted by the contractor using plate modelling for the purpose of data

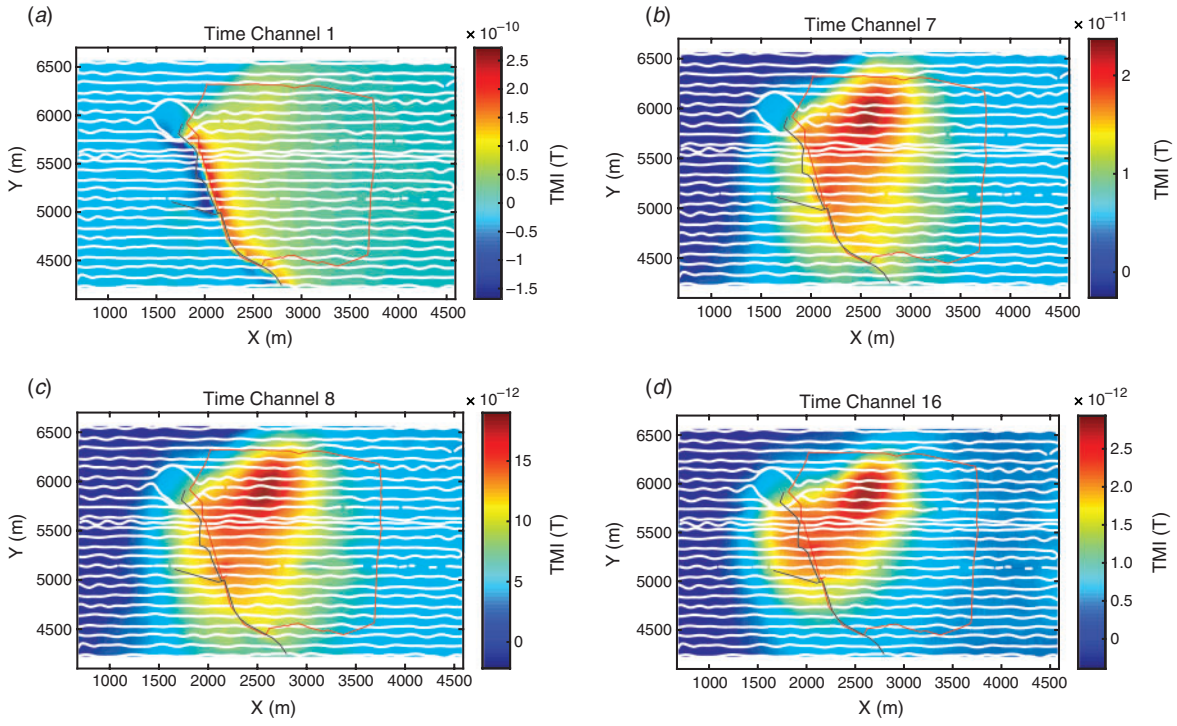

Fig. 3. HeliSAM data at Lalor: (*a*) Time Channel 1 at 0.42 ms, (*b*) Time Channel 7 at 3.33 ms, (*c*) Time Channel 8 at 4.38 ms and (*d*) Time Channel 16 at 27.7 ms. The transmitter loop, receiver lines and the power lines are indicated by the red, white and black lines respectively.

quality control, although no quantitative modelling result has been published. The noticeable irregular shape of the anomaly, and the peak on its northern tip, indicate that the target ore body can have complex geometry or orientation, or there is an undiscovered extension that we are not aware of. We believe that a full 3D voxel inversion is necessary to extract more complete information about the deposit and its surroundings.

It is often common practice in industry to discard data contaminated by infrastructure or other undesired noise, and only work with the reliable part of the dataset. In the following, we separate the HeliSAM time channels into two parts: the early-time part ranging from TC 1 to 7 that contain visible signals from infrastructure, and the late-time part from TC 8 to 16 that is dominated by the anomalies from the deep geologic target. We will first invert the late times to obtain a robust 3D conductivity model that shows the most important structure at the depth and scale appropriate for the Lalor deposit. Then the early times are considered in our inversion to provide additional constraints on the shallow structure and to reduce the non-uniqueness for the structure at depth.

3D modelling and inversion algorithms

The foundation of our 3D time-domain EM modelling and inversion is described in Oldenburg et al. (2013). The entire modelling domain is discretised into many cells on a 3D rectilinear mesh, and the quasi-static Maxwell's equations are solved using the finite volume method in space (Haber et al., 2000). The time integration is computed using the backward Euler (implicit time stepping) method. Our existing TEM code models three components of the magnetic field. In order to model TMI data, defined as the projection of the total induced magnetic field onto the direction of the earth's magnetic field, the 3-component vector of magnetic field must take the inner product with $\hat{\mathbf{B}}_0$, so the TMI is modelled as a linear combination of the three components of $\mathbf{B}_{em}$

$$d = \mathbf{B}_{em} \cdot \hat{\mathbf{B}}_0 = B_x \cdot \cos I \cdot \sin D + B_y \cdot \cos I \cdot \cos D - B_z \cdot \sin I, \quad (4)$$

where $(B_x, B_y, B_z)^T$ is the magnetic field vector, and the inclination and declination of the regional magnetic field are denoted by I and D respectively. Here we adopt a right-hand coordinate system with x pointing east, y pointing north and z pointing upwards. At Lalor, the inclination is 78° and the declination is 5.2°, so $\hat{\mathbf{B}}_0 = (0.15287, 0.14092, -0.97815)$, which means the HeliSAM measurements are almost the vertical component.

Following Tikhonov regularisation (Tikhonov and Arsenin, 1977), the objective function in our inversion can be expressed as

$$\underset{m,\beta}{\text{minimise}}\, \phi = \frac{1}{2}\phi_d(m) + \frac{\beta}{2}\phi_m(m), \quad (5)$$

where m is the sought model, ϕ_d is a functional of data misfit, ϕ_m is a regularisation term measuring the model norm, and β is a trade-off parameter. Different formulations can be used to construct ϕ_d and ϕ_m, but we choose the following based on L-2 norm. The data misfit is calculated as

$$\phi_d = \sum_{i=1}^{N} \left(\frac{d_i^{obs} - F_i(m)}{\varepsilon_i} \right)^2, \quad (6)$$

where N is the total number of data, $F(m)$ is the data predicted by the model m, d^{obs} is the observed data, and ε is the estimated uncertainty that weights the relative importance of individual datum. The model norm is

$$\phi_m = \alpha_s \int_\Omega \{w_s(m - m^{ref})\}^2 dv + \sum_{i=x,y,z} \alpha_i \int_\Omega \left\{ w_i \frac{\partial (m - m^{ref})}{\partial_i} \right\}^2 dv, \quad (7)$$

where Ω is the modelling domain, m^{ref} is a reference model, α_s, α_x, α_y, α_z are scalar weighting parameters adjusting the relative importance of different components in the model norm, and w_s, w_x, w_y, w_z are functions in 3D space that can fine tune the structural penalty at different places.

Expressing Equations 6 and 7 in discrete form, the objective function in Equation 5 can be written as

$$\phi = \frac{1}{2}\left\| \mathbf{W}_d \left[F(\mathbf{m}) - \mathbf{d}^{obs} \right] \right\|_2^2 + \frac{\beta}{2}\left\| \mathbf{W}_m \left(\mathbf{m} - \mathbf{m}^{ref} \right) \right\|_2^2, \quad (8)$$

where $\mathbf{W}_d$ is a diagonal weighting matrix of $1/\varepsilon_i$, $F(\mathbf{m})$ and $\mathbf{d}^{obs}$ are vectors of predicted and observed data respectively, and $\mathbf{W}_m$ is an assembly of one diagonal matrix and three directional first-order differential matrices with corresponding weights (α_s, α_x, α_y, α_z, w_s, w_x, w_y, w_z) coded. A Gauss–Newton (GN) method is used to iteratively minimise Equation 8. The model update $\delta\mathbf{m}^{k+1}$ at the kth GN iteration is obtained by solving

$$\left[\mathbf{J}(\mathbf{m}^k)^T \mathbf{W}_d^T \mathbf{W}_d \mathbf{J}(\mathbf{m}^k) + \beta \mathbf{W}_m^T \mathbf{W}_m \right] \delta\mathbf{m}^{k+1} = -\mathbf{J}(\mathbf{m}^k)^T \mathbf{W}_d^T \mathbf{W}_d \left[F(\mathbf{m}^k) - \mathbf{d}^{obs} \right] - \beta \mathbf{W}_m^T \mathbf{W}_m \left(\mathbf{m}^k - \mathbf{m}^{ref} \right), \quad (9)$$

where $\mathbf{J}(\mathbf{m}^k)$ is the Jacobian matrix of the model $\mathbf{m}^k$. Because the three components of the magnetic field are collapsed into TMI in the forward modelling of data (Equation 4), the sensitivity matrix of TMI data also requires a similar operation of linear combinations after the sensitivities of the three components are computed.

The general procedure of our inversion follows the cooling method in Haber (1997). First the inversion starts with an initial guess of the model and an over-estimated regularisation parameter β. Models at early iterations usually have simple structures and poor data fit. It may take a few GN iterations to achieve the stationary point of Equation 5 for a given β. Then β is reduced to allow more structure to be built into the model and better data fit. The inversion iterates until the data fit reasonably within a prescribed uncertainty level.

From practical point of view, the users' inputs, particularly the data uncertainty ε, the initial model m_0 and the reference model m^{ref}, are crucial to the success of the inversion. The data uncertainty is used to weight the data misfit. If a dataset has large dynamic range, the uncertainties are usually a percentage of the amplitude. Large uncertainties can be assigned if some data are intentionally down-weighted. The initial model should represent the users' best knowledge about the true model, as the mathematical assumption of nonlinear optimisation requires the initial guess sufficiently close to the true solution. The reference model is a way of effectively incorporating *a priori* information, because the model penalties in Equation 7 are only applied to the difference between the reference model m^{ref} and the current model m^k. Just as the initial model, the reference model should always be as close to the true model as possible. The importance of the reference model becomes significant when m^{ref} contains non-uniform structure, since any structure embedded in it has very strong influence on the output model of inversion. These aspects will be important in this paper.

Inversion preparation

Our workflow begins by finding a representative uniform half-space as the background that hosts the target. We use the field data in the region where no significant anomaly is present. A conductivity of 0.0014 S/m (or resistivity of 700 Ωm) is chosen for the best-fitting half-space. The primary use of this representative half-space value is to aid the design of the 3D mesh used in our voxel inversion program. The smallest cell size and domain size of the mesh are inferred using the diffusion length

$$d = \sqrt{\frac{2t}{\sigma\mu}}, \tag{10}$$

which implies the spatial scale of diffusion can be primarily determined by the delay time t and conductivity σ and the magnetic permeability μ (Nabighian and Macnae, 1991). The diffusion length of the earliest time is ~700 m and the smallest cells should be a fraction of that value. The diffusion length for the latest times is 5500 m and the domain size should be several times this value. We note that the conductive target can cause localised vortex currents at smaller scales but the conductors of concern at Lalor are at least a few hundred metres deep, so we have made the cell size 100 m in the core area that contains the transmitter and receivers. The distance between the survey border and the boundary of the modelling domain is chosen to be 10 km, about two times the largest diffusion length. This ensures that the prescribed no-flux boundary condition is satisfied. The region between the survey area and the outer boundary of the modelling domain is padded by cells that coarsen at a geometric rate.

For this particular dataset, we need to properly scale the signals that decay exponentially in time, down-weight the zero-crossing data that had an extremely small amplitude, and honour the better SNR when the receiver is directly above the target. This can be achieved by assigning different uncertainties to the data, and a representative half-space model can provide a good first-order reference to the magnitude. We use the actual survey geometry to generate synthetic data for the 0.0014 S/m half-space, then calculate 30% of the magnitude of induced magnetic field ($\mathbf{B}_{em}$) at each receiver and at each time, and use this as the uncertainty. This uncertainty is assigned for the following reasons. First, by using a percentage of the total field magnitude we ensure that we do not assign a zero uncertainty to a datum that is associated with a zero-crossing. Such data arise when a particular component is null-coupled because of orientation. Second, because the uncertainty is derived from an anomaly-free half-space, the actual uncertainty assigned to field data is ~5–10% at the peak anomaly, ~20–40% at the margins, and greater than 1000% for a few zero-crossing data. This reflects our desire to better fit the anomalous data that have large magnitude. We note that the 30% used here is subjectively chosen to reflect the relative data uncertainty within the dataset. It represents neither the actual measurement noise nor the goodness of data fitting in the inversion. As demonstrated in the following section, we may choose to fit the observed data better than this assumed uncertainty. Third, by using a substantial percentage of the total field, the assigned uncertainties were sufficiently large that an additive constant floor value was deemed unnecessary.

The uniform half-space itself is usually a reasonable starting and reference model in a 'blind' inversion when no specific *a priori* information is available. Our previous experience shows that inversions of EM induction data are usually able to recover a meaningful model from a half-space (e.g. Yang and Oldenburg, 2012*a*). We therefore use the 0.0014 S/m half-space as the initial and reference model in our preliminary blind inversion.

There are some other practical considerations when carrying out the 3D inversion. The topography at Lalor is almost flat, ranging from 280 to 320 m ASL. Because the variation of elevation is much smaller than the smallest scale of EM induction, we model the air–ground interface as a flat surface

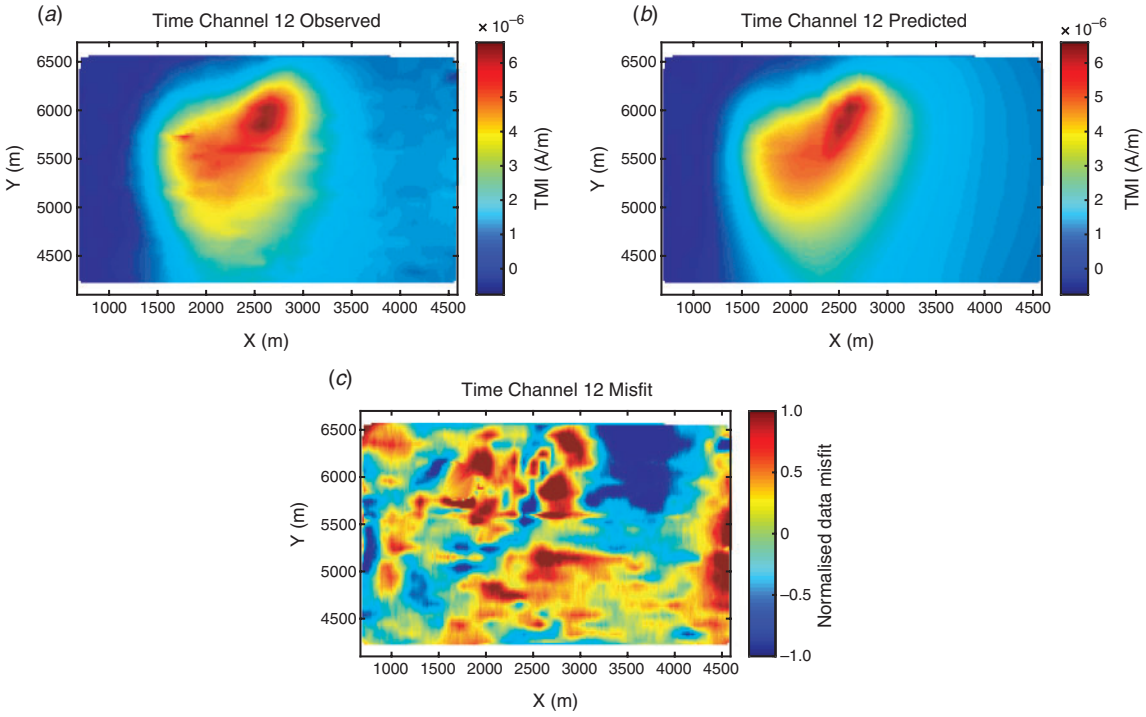

Fig. 4. Blind inversion of late-time HeliSAM data: (*a*) The observed data, (*b*) the predicted data, and (*c*) the data misfit normalised by the uncertainties.

at a constant depth level $z = 0$ (305 m ASL). The irregularly shaped transmitter loop is modelled as 70 current line segments connected in sequence on the surface. Because our inversion program takes H-field data as input, instead of B-field, the entire dataset is divided by the vacuum magnetic permeability $\mu_0 = 4\pi \times 10^{-7}$ H/m.

Inversion of late-time data

Blind inversion

As a first effort, we follow the common practice of discarding the contaminated data, and only invert TC 8 to 16 (4.4–28 ms) on a mesh with 100 m cells. The initial and reference models are both 0.0014 S/m half-spaces. Before any interpretation on the recovered model is made, we examine some metrics of the inversion. The first quantity is the overall data misfit in Equation 6, which, when plotted against the model norm, decreases monotonically (Figure 8). This type of Tikhonov curve reflects a continual transition from 'poor data fit and simple model' to 'good data fit and complex model'. If the exact uncertainty is known and correctly assigned to the data, the desired misfit (calculated as the data misfit in Equation 6 normalised by the total number of data) should be approximately unity. In our case, the true uncertainty is unknown and a nominal uncertainty has been assigned to the data, so an exact stopping criterion is not available. As such we allow the inversion to continue for more iterations after the unity of misfit is achieved.

The quality of inversion is quantitatively assessed in the following steps. First, the continued decrease of the Tikhonov curve is an overall indication of acceptable data misfits. However, the cooling method usually generates a series of models with similar structure and data misfits at the late iterations, and one model needs to be chosen for the interpretation. Second, we examine the spatial distribution of the data misfit by plotting the TC maps of the observed data, predicted data, and the normalised misfit. In addition to a good match between the observed data and the predicted data, a good model should not produce significant coherent residuals. Large-scale coherent data misfits are generally an indication that there is still information in the data that has not been extracted. Misfit maps are valuable in this regard and so are histograms of the normalised misfits. Models from later iterations often have better behaviour in the misfit, but at some point, additional structure that is not deemed geologic will appear because noise is being fitted. We therefore choose a model, from the earliest iteration possible, that has an acceptable misfit using the criterion above. For the blind inversion, we choose the model from the 18th GN iteration, whose observed data, predicted data and misfit are provided in Figure 4.

Now that the statistical evidence shows that the inversion has found a model that adequately reproduces the observations, we proceed with the geologic interpretation. Surprisingly, the recovered conductivity model contains structure that is not geologically meaningful. In particular, a substantial amount of conductive material is constructed on the margin or outside of the data area, and the location of the drilled ore lenses is imaged as a resistor (Figure 5).

The contradiction between the recovered structure and the expected geology reminds us that a mathematically acceptable model can sometimes be geologically erroneous. Although the non-uniqueness of geophysical inversions has long been acknowledged, especially for potential field data, a complete failure like this is surprising in EM inversions where there are many receiver locations and many time channels. Some plausible reasons for the discrepancy include:

- Limitation of data. The dataset only contains one fixed transmitter and only one component of the magnetic field in a narrow frequency band. Those allow many different ways of fitting the data, and make it difficult for the statistical quality control to recognise the problem.
- Improper scale of investigation. The diffusion lengths of TC 8 to 16, based on the initial model of half-space, are larger than the survey area and high sensitivity extends into the padding

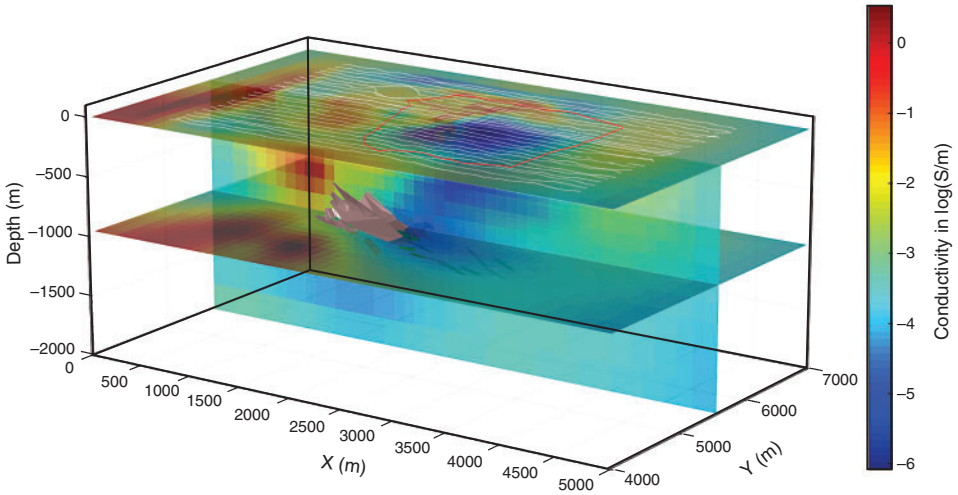

Fig. 5. Blind inversion of late-time HeliSAM data: recovered conductivity model. The red line and white lines on the surface indicate the HeliSAM transmitter and receivers respectively. The drilled ore lenses are presented in pink and green polyhedrons for reference.

Table 1. Specifications of the two conductive blocks used in the warm-start inversion.

Block	Range in X	Range in Y	Range in Z	Centre of mass (X, Y, Z)	Conductivity
#1 (green)	1758–2458	4885–5785	–650∼ –1050	(2108, 5335, –850)	1 S/m
#2 (yellow)	2550–2858	5450–6350	–450∼ –850	(2704, 5900, –650)	2 S/m

cells. The survey has decent coverage for the vortex currents in the small-scale conductive bodies, but the area is not large enough to constrain the structure in the padding cells when the inversion starts with a half-space whose responses are dominated by galvanic currents.

- Smooth model constraint. The larger-scale conductive structures away from the transmitter and receivers are favoured by the inversion because of their relatively small contribution to the model norm compared to a compact conductor that has sharp boundaries.
- Local linearisation in the optimisation. The high conductivity built up at an incorrect place in the first few iterations will increase the sensitivity in those cells in the next iteration. This positive feedback can prevent the inversion from correcting itself.

In principle, the items above are the result of imperfect data and inadequate *a priori* information, and they have a combined impact on the inversion models. For example, the initial half-space model overestimates the scale of investigation and positions the inversion at a bad starting point. A dataset that provides wide-band constraints on both the shallow and deep structure in a sufficiently large area may correct the structure created at the incorrect scale of investigation. Unfortunately, TC 8 to 16 of HeliSAM at Lalor are not capable of providing the necessary constraint. The smooth constraint in the inversion also further encourages smoothness in the model, instead of compactness required by the VMS deposit.

Warm-start inversion

The non-uniqueness of inversion can be improved by acquiring more data and/or incorporating more constraints. Here we propose a warm-start method that can be easily implemented without acquiring more data or alternating our algorithm. The basic idea is to adjust the scale of investigation by introducing strong conductors into the initial model close to the region where the deposit is situated. Because it only serves as a starting point, using such an initial model is considered as a soft constraint in the inversion. The task is therefore to find one or more conductors that can be inserted into our half-space of 0.0014 S/m. Many geometric inversion algorithms can help us find the locations, geometries and conductivities of those conductors (Keating and Crossley, 1990; Smith and Lee, 2002; Raiche, 2004; McMillan et al., 2015). We used MAXWELL software (Midland, Australia), a commercial program featuring plate modelling, because of its popular usage in the mining industry. The responses of a 0.0014 S/m half-space are first subtracted from the field data in order to isolate the anomaly as if the conductors are in free space. Then the anomalous data are roughly fit by two conductive blocks shown in Figure 6 and described in Table 1. The half-space-removed field data and the MAXWELL modelled data are compared along two flight lines in Figure 7.

Although the initial model now contains structure, we keep the reference model as the same half-space model. Thus, the two blocks in the model are still subject to the same model norm as in the blind inversion. This represents minimum *a priori* information and the weakest constraint one can incorporate into the inversion and it also serves our purpose for comparing two inversion results. As the inversion proceeds, the trajectory of iterations on the Tikhonov plot becomes a 'C-curve' as the upper part represents the simultaneous reduction of data misfit and model norm (Figure 8). This happens if the initial and reference models are different and the initial model contains unfavoured structure. Eventually, with successive iterations the sharp boundaries in the initial model are smoothed out, and the inversion starts to build other structure necessary to fit the data. This generates the lower part of the C-curve. The comparison of the two Tikhonov curves corresponding to the blind and warm-start inversions suggests that the latter explored a different portion of the model space.

The final model is chosen using the same criterion of incoherent misfit residual. The predicted data of this warm-start inversion is not significantly different from the predicted data of the blind inversion (Figure 9), but the new model has a

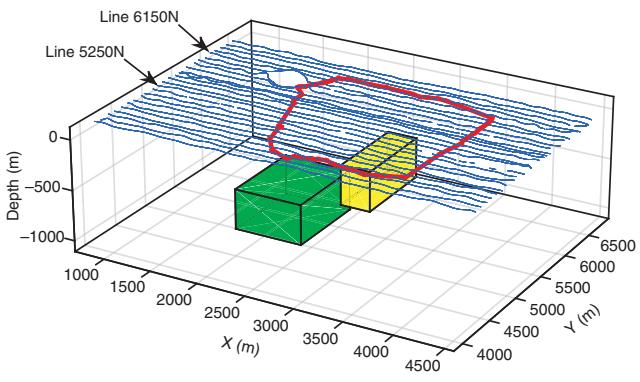

Fig. 6. The two blocks of the initial model used in the warm-start inversion. The red line and blue lines on the surface indicate the HeliSAM transmitter and receivers respectively.

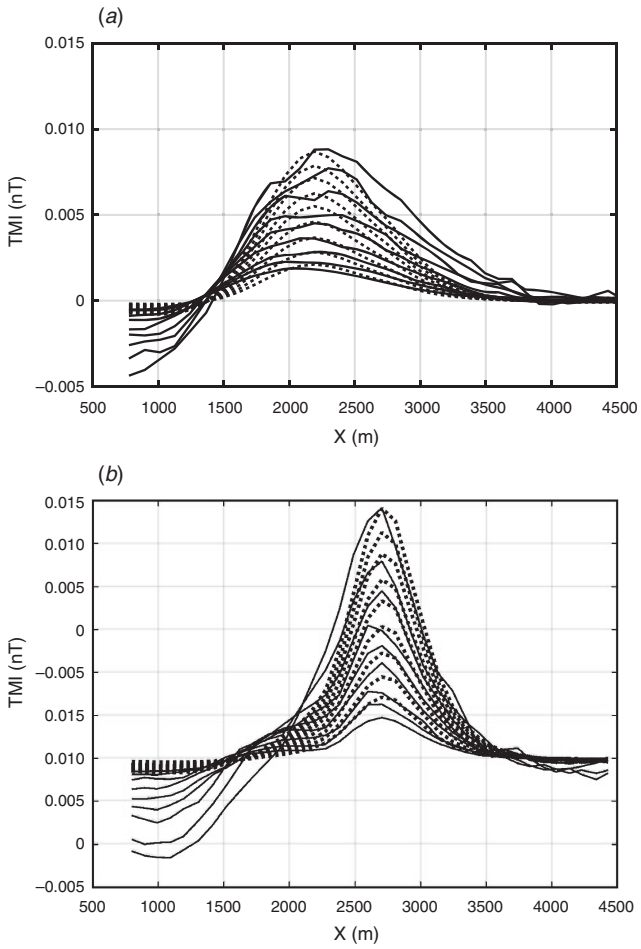

Fig. 7. The HeliSAM field data after half-space removal (solid lines) and the MAXWELL modelled data of the two blocks in free space (dotted lines). Two flight lines at Time Channels 8–16 are shown: (*a*) Y = 5250 m and (*b*) Y = 6150 m.

completely different structure that resembles a complex of compact and conductive ore bodies at the expected position (Figure 10). The conductive bodies found in the padding cells in the blind inversion are no longer present in the new model. This field example reminds us how a totally incorrect model can be produced by inversions and, in addition to the statistic metrics, geophysicists also need geologic validation of the model before the result can be useful for the interpretation.

Inversion of early-time data

Inverse approach

The warm-start inversion of the late-time data successfully recovered the major conductors, but it also revealed other near surface conductive features of geologic interest (see the slice at depth = 0 in Figure 10). The existence of those conductors is questionable because they are smaller than the scale of investigation of the late times and data may still have had contamination from infrastructure that was not accounted for. We therefore turn attention to the early-time data. The major difficulty of inverting the early times of the HeliSAM data is that those data contain large signals from the surficial infrastructure that shadow the useful signals from the geologic targets. Therefore, in order to utilise the early-time data, the responses from the infrastructure must be properly accounted for.

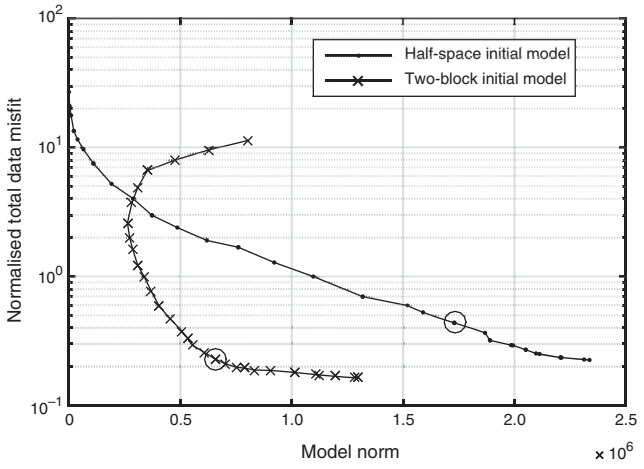

Fig. 8. Tikhonov curve of the blind inversion starting from a half-space and the warm-start inversion starting from two blocks in half-space. The circles mark the Gauss-Newton iterations from which the final models are obtained.

The infrastructure can generate anomalous data as active source or passive conductors. The linear pattern on the early data maps corresponds well with the trace of power line, which is usually a particular concern in geophysical surveys (Butler and Russell, 2003; Legchenko and Valla, 2003; Saucier et al., 2006; Cohen et al., 2010). We determined at Lalor that the time varying current in the power line has a negligible effect in the HeliSAM data because the system has been carefully designed to minimise the interference at 60 Hz. The transmitter base frequency used in this survey is a sub-multiple of 60 Hz, so any signal from the 60 Hz current can be stacked out by using a bipolar waveform (Mal Cattach, 2015, pers. comm.). There is no other active current source we can identify at Lalor. On the other hand, the infrastructure can be constructed with good conductors, for example, the metal wires in the power lines and the metal parts used to build the towers, pipelines, head frames and other buildings. Those objects are small compared to the geologic targets, but they are highly conductive and close to the transmitter wire and receivers (Yin and Wang, 2015). Their EM signature has a high response at the early-time and decays quickly; this emulates what we have observed in the HeliSAM field data. As a result, we will treat the infrastructure, including the power line, as near-surface conductors in our modelling.

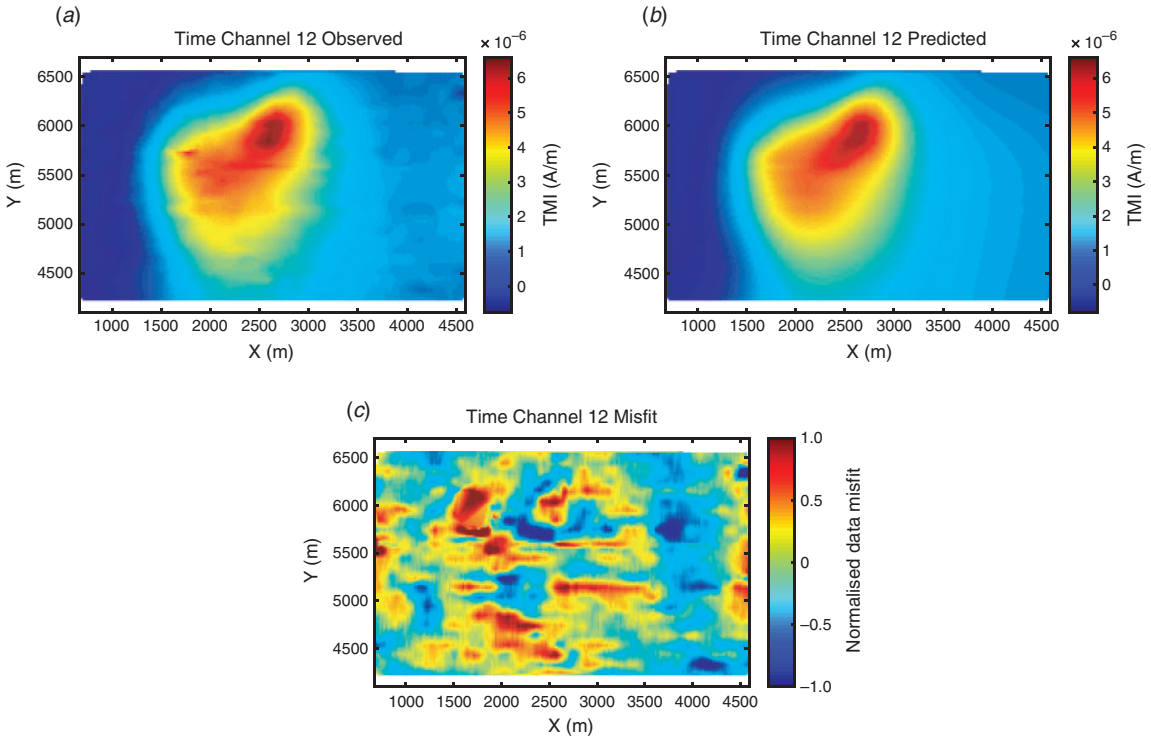

Fig. 9. Warm-start inversion of late-time HeliSAM data: (*a*) The observed data, (*b*) the predicted data, and (*c*) the data misfit normalised by the uncertainties.

There are two approaches to model the conductive infrastructure. The forward approach requires the exact information about the infrastructure, including the conductivity, geometry, location and grounding conditions, to accurately compute its EM responses. The modelled responses then can be taken into account in the subsequent inversions by either subtracting them from the field data or adding them to the modelled data. The forward approach is straightforward to implement, especially when treating the simple and isolated objects like steel casings (Wu and Habashy, 1994; Rucker et al., 2010; Commer et al., 2015; Um et al., 2015), but it is impractical for this dataset. First, we do not have precise information about the entire infrastructure that existed at Lalor when the survey was carried out. Second, voxel modelling of thin objects needs extremely fine discretisation, which can be computationally challenging (Commer et al., 2015). Lastly, because receivers are very close to the infrastructure, the flight height and topography must be known precisely. As a result, we adopt an inverse approach that relies on inversion to recover an effective conductivity of the infrastructure. The most significant advantage of the inverse approach is that it lumps many unknown objects that are difficult to model together, and the voxel model allows the effective conductivity to change at different portions of the infrastructure. However,

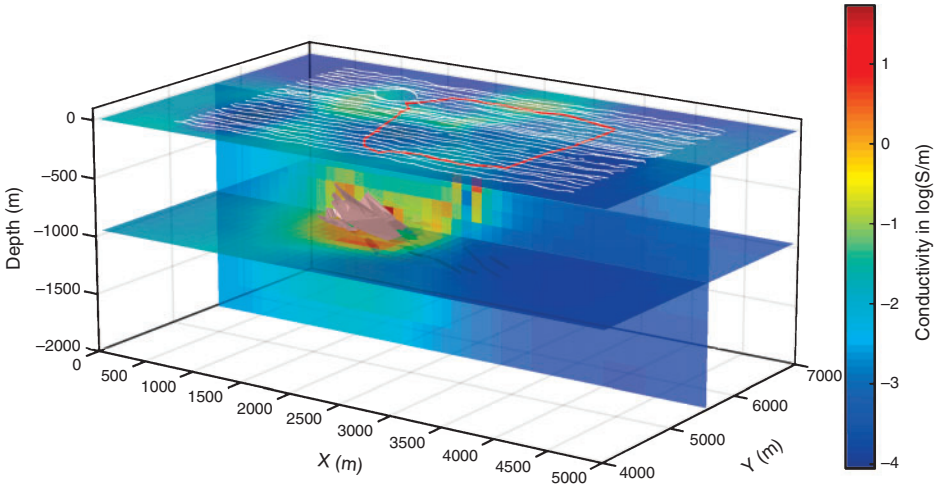

Fig. 10. Warm-start inversion of late-time HeliSAM data: recovered conductivity model. The red line and white lines on the surface indicate the HeliSAM transmitter and receivers respectively. The drilled ore lenses are presented in pink and green polyhedrons for reference.

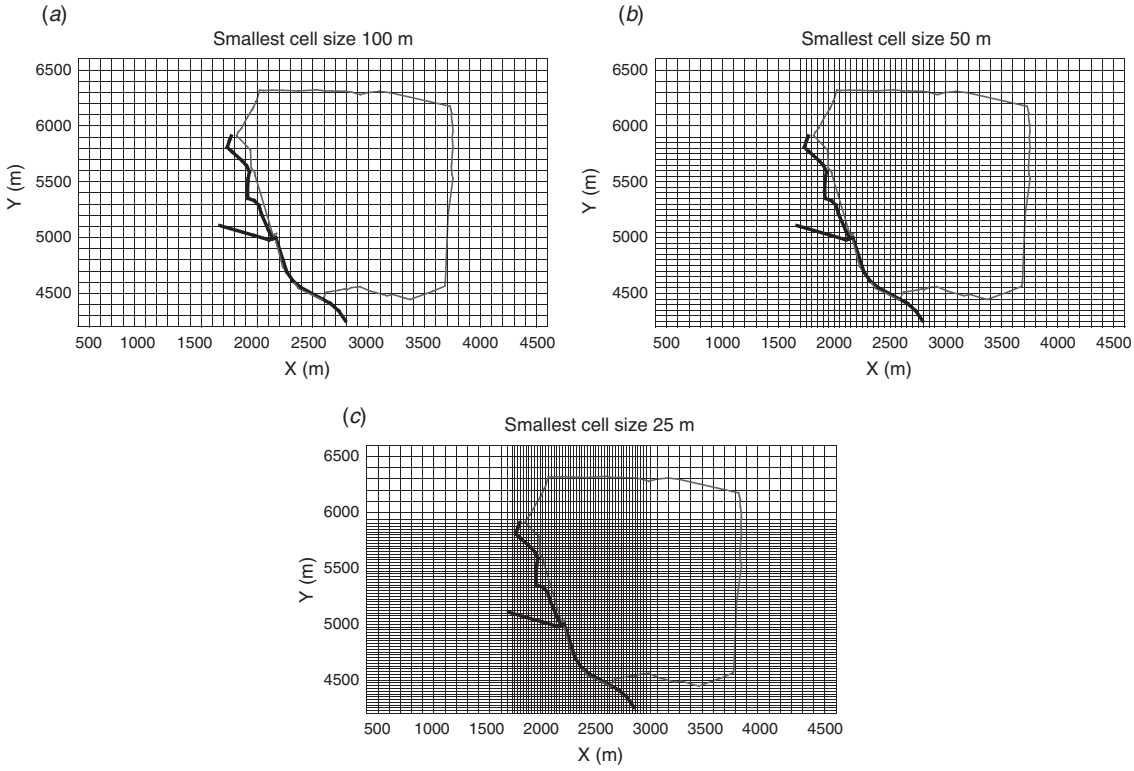

Fig. 11. Trial meshes with the smallest cell size 100, 50 and 25 m. The padding cells are not shown. The thin line and thick lines indicate the HeliSAM transmitter and the power line locations in document respectively.

due to the intrinsic non-uniqueness of inversion, some advanced implementations are necessary. These are described in the following.

Mesh refinement

Modelling infrastructure, especially items like compact highly conductivity wires, might best be carried out with algorithms that use unstructured or semi-structured meshes (Davis and Li, 2013; Jahandari and Farquharson, 2014; Um et al., 2015) and implements non-L-2 measures of smoothness (Farquharson, 2008; Sun and Li, 2014). Here, however, we show that commonly used software, employing highly structured rectilinear meshes, can be adequate. Since the inverse approach looks for an effective conductivity that gives rise to the equivalent EM responses, the mesh does not need to be discretised as fine as the actual geometry of the object. The 3D mesh with 100 m cell used in the late-time inversion is not likely to be fine enough because the signals observed in the earliest time channels can vary from the negative maximum to positive maximum within spatial scales of less than 100 m; this is due to the surface infrastructure. In order to determine the smallest cell size for modelling the infrastructure, we run trial inversions on the meshes with consecutively refined cells and select that size where the inversion results are no longer affected by further reduction in cell size.

The 100 m cell mesh is first used in the inversion of TC 1 to 7 (0.4–3.3 ms) with the initial and reference model both half-spaces of 0.0014 S/m. Cells within a box that encloses the infrastructure anomaly are refined twice, yielding one mesh with 50 m cells and another with 25 m cells (Figure 11). Two additional inversions, with identical inversion parameters, are run using these meshes. The inversions achieve different levels of misfit: the 100 m cell mesh is not able to adequately reduce the misfit and there is significant leftover signal in the data that cannot be fit when the flight line crosses the power line; the 50 m and 25 m cell meshes have similar performance in terms of resolving the fine-scale anomalies (Figure 12) and in fitting the data. We conclude that a 50 m cell mesh should be fine enough to estimate an effective conductivity of the infrastructure.

Infrastructure boundary sharpening

The surface conductivity recovered by the trial inversion using the 50 m cell mesh shows a very clear linear feature that resembles a major power line with a side branch (Figure 13*a*). Another surficial conductor having a moderate conductivity and significant depth extent, and cutting the top-left corner of the transmitter loop, is more likely a geologic feature. Our inversion model is indicative of the location of the conductor near the surface, but the recovered infrastructure is smeared out because of smoothness constraints in our inversion algorithm.

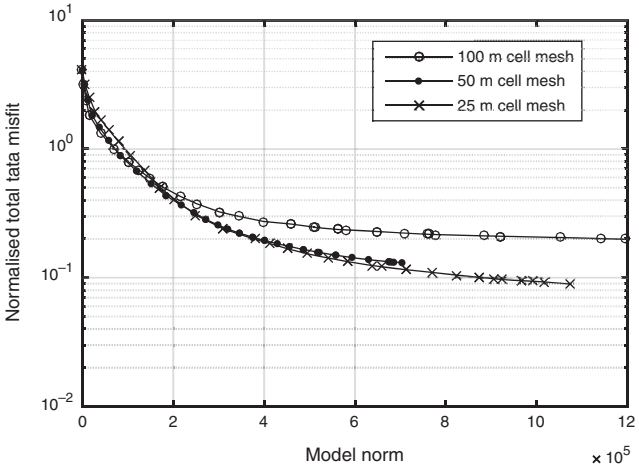

Fig. 12. Tikhonov curves of the three trial inversions using different smallest cell sizes.

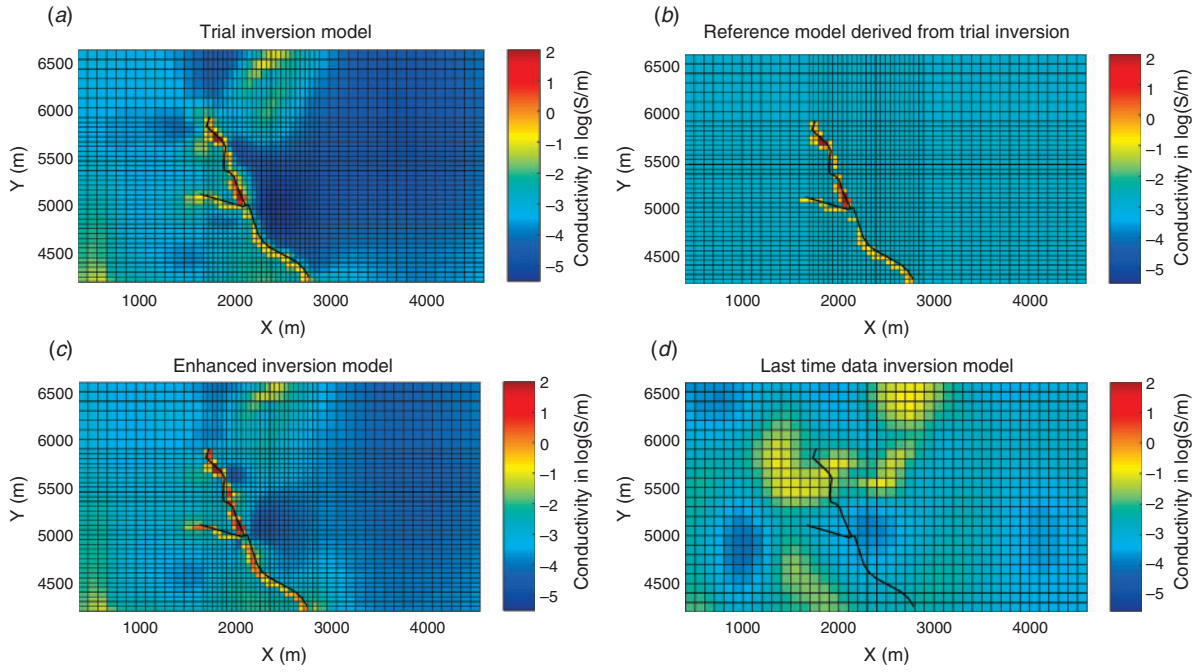

Fig. 13. Recovery of the effective conductivity on the surface for the infrastructure. (*a*) A trial inversion of early-time data using a half-space as the initial and reference models is first carried out. (*b*) A non-smooth initial and reference model is made from the trial inversion model for the boundary sharpening. (*c*) The early-time data are inverted again using the non-smooth initial and reference model. (*d*) Only inverting late-time data can result in unrealistic near-surface structure. The location of the power line is indicated by the black line segments.

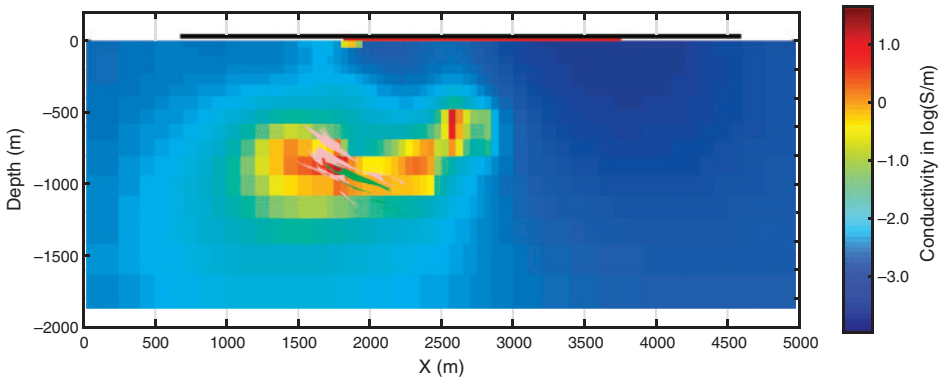

Fig. 14. Cross-section at Y = 5600 m of the all time inversion model obtained using the infrastructure effective conductivity recovery and warm start. The drilled ore lenses are shown as the pink and green polygons. The red line and black line on the surface indicate the HeliSAM transmitter loop and the receiver line respectively.

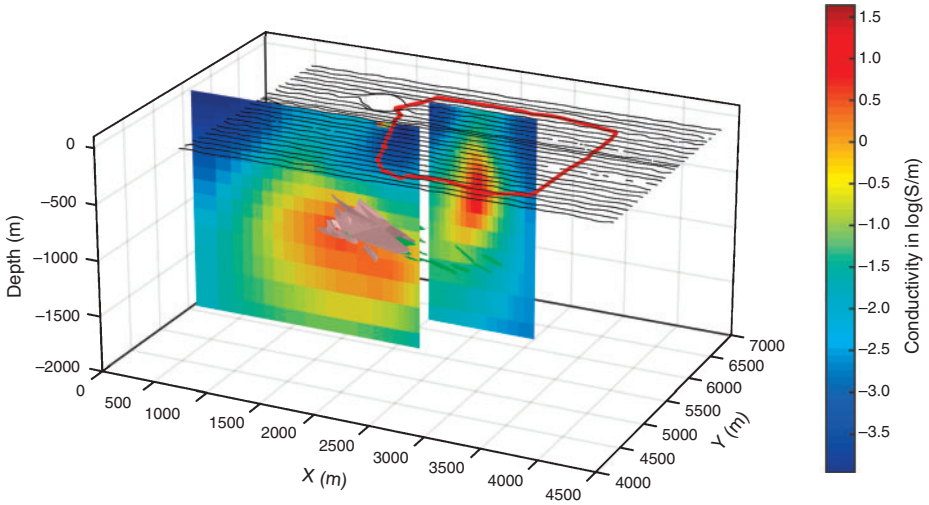

Fig. 15. Inversion of all times starting from a uniform initial model for the geologic targets. The model is shown at two cross-sections Y = 5600 and 6100 m. The red line and black lines indicate the HeliSAM transmitter and receivers lines respectively.

We might expect sharp boundaries between the metal objects and the earth. As part of our workflow we next sharpen the infrastructure so that the artificial objects are more isolated from the naturally occurring objects; this may reduce the risk of misinterpretation.

Different methods can be used to recover sharper boundaries in a voxel inversion, for example, by using non-L-2 measure in the model norm, or reducing the relative weight of components of a model norm on the boundaries. Here, without altering the algorithm, we adopt an 'iterative Tikhonov' approach that uses an updated reference model for each step in the inversion. Because the penalty for the conductivity contrast is applied to the difference between the current model and the reference model, any existing structure in the reference model is not penalised when evaluating the model norm. Thus any structure encoded in the reference model will continue in the inversion unless it has to be modified to fit the data.

We take the recovered model from the 50 m cell mesh inversion (Figure 13*a*), and isolate the conductive cells (greater than 0.05 S/m) near the surface (shallower than 300 m) in the area where the infrastructure is expected. The initial and reference model for the constrained inversion is then made by

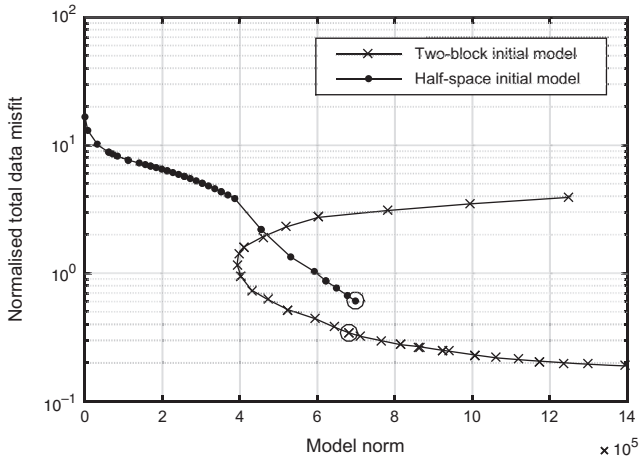

Fig. 16. Tikhonov curves of all-times inversions with and without warm start of the two blocks in the initial model. The initial and reference models always contain the surficial conductive cells for the infrastructure. The circles mark the Gauss-Newton iterations from which the inversion models are obtained.

embedding those conductive cells in a 0.0014 S/m half-space (Figure 13*b*). This reference model is included in the smoothness term of the model norm so the existing structure does not count towards the complexity of the model. The constrained inversion, with the same parameters used in the trial inversion, recovers sharpened features with enhanced conductivity (Figure 13*c*). For the most part, the surficial conductors have high conductivity no more than a couple of cells deep and wide, indicating the infrastructure could be mostly thin objects; for example, a pipe line or power line. However, there are two places on the linear trace, one at the conjunction of the main route with the branch, and the other at the northern end of the main route, that show high conductivity in a larger volume that is more deeply buried. These are likely to be other types of infrastructure of greater size, like buildings or head frames.

We now compare the surface conductivity obtained with the late-time inversion (TC 8–16) and early-time inversion (TC 1–7). The late-time data do not appear to contain contaminated signal but the residual responses from the infrastructure can still be responsible for the occurrence of conductive material on the surface (Figure 13*d*). In contrast to the common belief that discarding bad data is a safe practice, this example shows that an inversion may have higher risk of producing misleading structure if the data are incomplete, and geophysicists should model the dataset as completely as possible.

Inversion of all times

Now that a good representation of the infrastructure has been obtained we can invert our full dataset that has 16 time channels. The initial model includes the highly conductive near-surface cells recovered as the infrastructure and the two conductive blocks at depth used for the warm start. The reference model only contains the infrastructure cells and the background cells are set to 0.0014 S/m. The inversion again exhibits a C-curve on the Tikhonov plot of model norm versus misfit (Figure 16). After 15 GN iterations an acceptable misfit, with no significant coherent residual, is obtained. The inversion recovers three conductive objects in the model (Figure 14). The most important feature is a dipping thin conductor; this is in very good accordance with the drilled ore lenses. There is another, nearly vertical, conductor that is smaller in size and shallower in depth (X ≈ 2600 m in Figure 14). There was some indication of this obtained from the geometric inversion (see the yellow-coloured block in Figure 6). This conductor extends to the north and eventually crops out as a smeared conductive feature for Y > 6000 m (see the surface conductivity in Figure 13*c*). Recent drilling has confirmed that this vertical conductor is a sulphide-bearing argillite, and some sections of it are highly conductive (Brian Taylor, 2015, pers. comm.). The third conductor on the cross-section is the effective conductivity cells of the infrastructure, which are only one cell thick and a few cells wide (X ≈ 1900 m in Figure 14).

Discussion

The Lalor HeliSAM dataset offers an opportunity to examine non-uniqueness in EM inversion. The non-geologic model obtained when beginning with a half-space and inverting late-time data was largely attributed to the limitation of data. Initiating the inversion with a warm start allowed a satisfactory result to be obtained. Since we have effectively modelled the infrastructure using early-time data, we can explore whether inclusion of the early-time data might allow us to omit the warm start from the procedure. We carry out a test inversion exactly as the previous inversion using all of the times, except that the starting model is a half-space with surficial infrastructure cells. Without a warm start for the geologic targets, the inversion was able to recover a model that is moderately reasonable geologically. There is a confined conductor at depth, but the conductor is smooth and is more deeply buried than the ore lenses model and the warm-start inversion result (Figure 15). The recovery of the vertical and small conductor has the similar issue of being larger, smoother and deeper than that from the warm-start inversion. We attribute this improvement over the blind inversion result to the fact that the additional early-time data provided more information about the smaller-scale model structure, although this test inversion still suffers from the improper starting model and smoothness constraints.

We can assess the quality of this test inversion using the metrics previously used. The Tikhonov curve of the test inversion is compared with that from the final warm-start inversion (Figure 16). For the same value of the model norm, the warm-start inversion achieved an acceptable misfit after 15 GN iterations, while the inversion starting from a half-space, and after 30 GN iterations, achieved a misfit that is two times greater. The warm-start inversion is more efficient at introducing structure that reduces misfit and this is evidenced in the data misfit map (Figure 17). The warm-start inversion generates a more random misfit map, whereas the misfit for the test inversion shows coherent signal, a bullseye that is a typical pattern when a sharp peak in the data is underfit. Although the test inversion has a reasonable total data misfit on the Tikhonov curve, the associated model is inferior.

We also tried other test inversions in an attempt to recover a reasonable model from a starting model that did not have the two conductive blocks. Since we expect the conductor to be located near the peak of the data anomaly, we forced the inversion to only build structure within a predefined volume. This was done by setting cells outside a prescribed volume to be

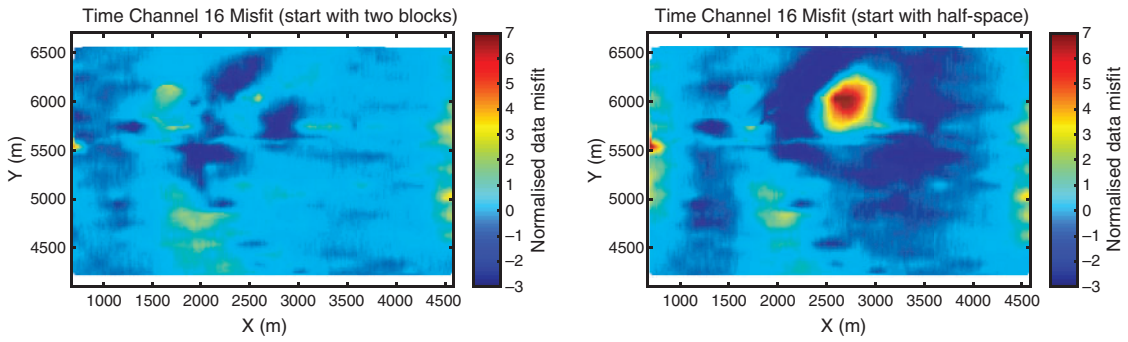

Fig. 17. Data misfit maps of all-times inversions with and without warm start of the two blocks in the initial model. The initial and reference models always contain the surficial conductive cells for the infrastructure.

inactive or applying reweighted model norm that prefers structure within that volume. Both constrained inversions lead to models that were inconsistent with the geology. Again, however, these models had an acceptable overall misfit, but the algorithm struggled to achieve that value, and also the residuals were coherent and had signal like a bullseye over top of the true geologic body.

We believe that the bullseye pattern in the misfit reflects that the data, produced mostly by vortex currents confined in compact bodies, are difficult to generate when starting from a uniform or smooth model in which the currents are predominantly galvanic in origin. When the inversion starts from a half-space, the resultant models are biased towards longer wavelength. For models associated with lower conductivity contrasts, such as disseminated sulphides in porphyry deposits, the bias can be overcome in a few iterations, and a fairly compact body can be obtained, especially if using non-L-2 measures in the objective function. However, the discrete good conductors associated with massive sulphides buried in a resistive background, require a conductivity that is different from a half-space for a linearisation technique to work satisfactorily. The warm start provides short-wavelength components in the initial model, so even though the two blocks do not necessarily represent the correct conductivity interface, the inversion is able to get to a more correct geologic answer. We have found, using additional tests, that even very rough guesses, like conductive spheres, can provide a sufficiently good initial model.

Conclusions

The Lalor deposit is a world-class VMS that has both great economic value and a geophysical signature that has made it a valuable test site for EM geophysical surveys. One of the datasets collected at Lalor is HeliSAM, a time-domain EM survey employing a large fixed ground loop and an airborne total B-field receiver. HeliSAM combines the merits of surface and airborne EM, offering a large transmitter moment (better SNR) and regional data coverage; it is well suited for deep targets like Lalor. In this paper, we interpret this dataset using a 3D voxel inversion technique. In order to model HeliSAM data, we modified our existing code that computes the three-component magnetic field (B-field) by projecting the modelled vector field onto the earth's regional magnetic field. We demonstrated the difficulties encountered when inverting the data and present solutions, in terms of a workflow, that can be adopted by the practitioners for use in similar situations.

First, the early times were largely contaminated by the infrastructure, probably the power line and metal buildings. Although it is the common practice to discard 'bad' data associated with early-time distortions, there is invaluable information in those data and our finite volume modelling is able to include the infrastructure as part of the conductivity model. Different approaches exist. The forward approach can be used, but it requires accurate information about the infrastructure, which is hard to know in reality. We prefer to invert for an effective conductivity for the surficial cells from the data. Our workflow for the inverse approach includes two steps: (1) trial inversions on meshes using successively smaller cells to find the largest size of the cell that can be used to effectively represent the non-geologic signal from the infrastructure. In our case, 50 m cells were satisfactory for the inversion of surficial effective conductivity even though the infrastructure may have dimensions of centimetres. (2) We invert the early-time data, use the recovered high conductivity cells at shallow depths to generate an infrastructure-included reference model, and perform another constrained inversion to recover the conductivity for the rest geologic structure.

The other difficulty is the recovery of the deep conductor that has a compact shape. Voxel 3D inversions often start from a representative uniform half-space. However, if only late times are inverted, the inversion produces a model that mathematically fits the data but is non-geologic. By including more data from the early times, the inversion slowly converges to a more reasonable model but the recovered conductor appears deeper, larger and weaker. We conclude this reflects the difficulty of recovering a compact conductor with sharp interface at depth from a smooth model. Our solution is to warm-start the inversion by introducing provisional conductors into the initial model. When inverting only late-time data we use a geometric inversion algorithm (MAXWELL) to generate two conductive blocks and bury them in a uniform background as the initial model. This warm start significantly speeds up the convergence of inversion, and can avoid long-wavelength bias of the model. In the final inversion that uses all time channels, the initial model contains the effective conductivity of the infrastructure and the two blocks. The final model shows the near surface conductivity associated with infrastructure and geology, and two important geologic conductors at Lalor: the main stack of ore lenses at depth consistent with the drilled near-solid and stringer sulphides and another shallower, smaller and vertical sulphide-bearing argillite that was also confirmed by recent drilling.

Acknowledgements

The authors thank the sponsoring companies of UBC-Geophysical Inversion Facility and NSERC for the funding. Roman Shekhtman provided assistance with the software programming. The field HeliSAM data at Lalor was provided courtesy of Hudbay Minerals Inc. and Gap Geophysics. Mal Cattach provided technical information about the HeliSAM survey at Lalor. We thank Andrew Duncan from ElectroMagnetic Imaging Technology Pty Ltd for providing a copy of their MAXWELL software. The authors also benefitted from the Lalor Symposium organised by the British Columbia Geophysical Society in 2014.

References

Butler, K. E., and Russell, R. D., 2003, Cancellation of multiple harmonic noise series in geophysical records: *Geophysics*, **68**, 1083–1090. doi:10.1190/1.1581080

Cohen, M. B., Said, R., and Inan, U., 2010, Mitigation of 50–60 Hz power line interference in geophysical data: *Radio Science*, **45**, RS6002. doi:10.1029/2010RS004420

Commer, M., Hoversten, G. M., and Um, E. S., 2015, Transient-electromagnetic finite-difference time-domain earth modeling over steel infrastructure: *Geophysics*, **80**, E147–E162. doi:10.1190/geo2014-0324.1

Davis, K., and Li, Y., 2013, Efficient 3D inversion of magnetic data via octree-mesh discretization, space-filling curves, and wavelets: *Geophysics*, **78**, J61–J73. doi:10.1190/geo2012-0192.1

Farquharson, C. G., 2008, Constructing piecewise-constant models in multidimensional minimum structure inversions: *Geophysics*, **73**, K1–K9. doi:10.1190/1.2816650

Haber, E., 1997, Numerical strategies for the solution of inverse problems: Ph.D. thesis, University of British Columbia.

Haber, E., Ascher, U., Aruliah, D., and Oldenburg, D., 2000, Fast simulation of 3D electromagnetic problems using potentials: *Journal of Computational Physics*, **163**, 150–171. doi:10.1006/jcph.2000.6545

Jahandari, H., and Farquharson, C. G., 2014, A finite-volume solution to the geophysical electromagnetic forward problem using unstructured grids: *Geophysics*, **79**, E287–E302. doi:10.1190/geo2013-0312.1

Keating, P. B., and Crossley, D. J., 1990, The inversion of time-domain airborne electromagnetic data using the plate model: *Geophysics*, **55**, 705–711. doi:10.1190/1.1442882

Legchenko, A., and Valla, P., 2003, Removal of power-line harmonics from proton magnetic resonance measurements: *Journal of Applied Geophysics*, **53**, 103–120. doi:10.1016/S0926-9851(03)00041-7

McMillan, M. S., Schwarzbach, C., Haber, E., and Oldenburg, D. W., 2015, 3D parametric hybrid inversion of time-domain airborne electromagnetic data: *Geophysics*, **80**, K25–K36. doi:10.1190/geo2015-0141.1

Nabighian, M. N., and Macnae, J. C., 1991, Time domain electromagnetic prospecting methods, *in* M. N. Nabighian, ed., *Electromagnetic methods in applied geophysics, volume 2 – applications*: Society of Exploration Geophysicists, 427–520.

Oldenburg, D. W., Haber, E., and Shekhtman, R., 2013, Three-dimensional inversion of multisource time domain electromagnetic data: *Geophysics*, **78**, E47–E57. doi:10.1190/geo2012-0131.1

Raiche, A., 2004, Practical 3D airborne EM inversion in complex terranes: ASEG Extended Abstracts, 2004, 1–4.

Rucker, D. F., Loke, M. H., Levitt, M. T., and Noonan, G. E., 2010, Electrical-resistivity characterization of an industrial site using long electrodes: *Geophysics*, **75**, WA95–WA104. doi:10.1190/1.3464806

Saucier, A., Marchant, M., and Chouteau, M., 2006, A fast and accurate frequency estimation method for canceling harmonic noise in geophysical records: *Geophysics*, **71**, V7–V18. doi:10.1190/1.2159063

Smith, R., and Annan, P., 1998, The use of B-field measurements in an airborne time-domain system: Part I. Benefits of B-field versus dB/dt data: *Exploration Geophysics*, **29**, 24–29. doi:10.1071/EG998024

Smith, R. S., and Lee, T. J., 2002, The moments of the impulse response: a new paradigm for the interpretation of transient electromagnetic data: *Geophysics*, **67**, 1095–1103. doi:10.1190/1.1500370

Sun, J., and Li, Y., 2014, Adaptive Lp inversion for simultaneous recovery of both blocky and smooth features in a geophysical model: *Geophysical Journal International*, **197**, 882–899. doi:10.1093/gji/ggu067

Taylor, C., 2014, Mine scale description of the mineralization at the Lalor deposit, Snow Lake, Manitoba, Canada: *Proceedings from Exploration for Deep VMS Ore Bodies: The HudBay Lalor Case Study*, British Columbia Geophysical Society 2014 Fall Symposium, 1–3.

Tikhonov, A., and Arsenin, V. Y., 1977, *Methods for solving ill-posed problems*: John Wiley and Sons, Inc.

Um, E. S., Commer, M., Newman, G. A., and Hoversten, G. M., 2015, Finite element modelling of transient electromagnetic fields near steel-cased wells: *Geophysical Journal International*, **202**, 901–913. doi:10.1093/gji/ggv193

Wu, X., and Habashy, T. M., 1994, Influence of steel casings on electromagnetic signals: *Geophysics*, **59**, 378–390. doi:10.1190/1.1443600

Yang, D., and Oldenburg, D. W., 2012*a*, Three-dimensional inversion of airborne time-domain electromagnetic data with applications to a porphyry deposit: *Geophysics*, **77**, B23–B34. doi:10.1190/geo2011-0194.1

Yang, D., and Oldenburg, D. W., 2012*b*, Three-dimensional inversion of SQUID TEM data at Lalor Lake VMS deposit: SEG Technical Program Expanded Abstracts 2012, Society of Exploration Geophysicists, 1–5.

Yang, D., and Oldenburg, D. W., 2013, 3D conductivity model of the Lalor Lake VMS deposit using ground and airborne EM data: ASEG Extended Abstracts 2013, 23rd Geophysical Conference: Australian Society of Exploration Geophysicists, 1–4.

Yin, C., and Wang, R., 2015, Power line ground resistance detection using helicopter electromagnetic systems: *Geophysics*, **80**, E125–E133. doi:10.1190/geo2014-0421.1